# Influence of Irregular Coastlines on a Tornadic Mesovortex in the Pearl River Delta during Monsoon Season. Part I: Prestorm Environment and Storm Evolution

Lanqiang Bai*[1], Zhiyong Meng[2], Dan Yao*[3], Yu Zhang[4], Xianxiang Huang[5], Zhaoming Li[5], Xiaoding Yu[6]

[1] *Foshan Tornado Research Center, and China Meteorological Administration Tornado Key Laboratory, Guangdong Meteorological Service, and Southern Marine Science and Engineering Guangdong Laboratory (Zhuhai), Guangdong, China*

[2] *Department of Atmospheric and Oceanic Sciences, and China Meteorological Administration Tornado Key Laboratory, School of Physics, Peking University, Beijing, China*

[3] *Meteorological Observation Centre, CMA, Beijing, China*

[4] *Guangzhou Meteorological Observatory, CMA, Guangdong, China*

[5] *China Meteorological Administration Tornado Key Laboratory and Foshan Tornado Research Center, CMA, Guangdong, China*

[6] *China Meteorological Administration Training Center, CMA, Beijing, China*



Submitted to *Advances in Atmospheric Sciences on 15 May 2023*

Revised version 1: 6 September 2023

Revised version 2: 18 October 2023

* Corresponding authors: Dr. Lanqiang Bai (bailanqiang@foxmail.com)
Dr. Dan Yao (yaod@cma.gov.cn)

**Article Highlights:**

• Convergent boundary routinely forms on the west coast of the trumpet-shaped Pearl River Delta during the summer monsoon season.

• The tornadic mesovortex develops over the triple point where storm-generated cold outflows intersect with the convergent boundary along the west coast.

• The triple point is an important ingredient in the formation of rotating storm under the influence of the unique land–sea contrast, monsoon, and storm cold outflows.

## ABSTRACT

The Pearl River Delta (PRD), a tornado hotspot, forms a distinct "trumpet" shape coastline that concaves toward the South China sea. During the summer monsoon season, low-level southwesterlies over the PRD sea surface tend to be turned toward the west coast, constituting a convergent wind field along with the land-side southwesterlies which influences regional convective weather. This two-part study explores the roles of this unique land–sea contrast of trumpet-shaped coastline in the formation of a tornadic mesovortex within monsoonal flows in this region. Part I primarily presents observational analyses of prestorm environments and storm evolutions. The rotating storm developed in a low-shear environment (not ideal for supercell) under the interactions of three airmasses in the influence of the land–sea contrast, monsoon and storm cold outflows. This intersection zone ("triple point") is typically characterized by local enhancements of ambient vertical vorticity and convergence. Based on a rapid-scan X-band phased-array radar, finger-like echoes were recognized shortly after the gust front intruding the triple point. Developed over the triple point, they rapidly wrapped up with a well-defined low-level mesovortex. It is thus presumed that the triple point may have played roles in the mesovortex genesis, which will be demonstrated in Part II with multiple sensitivity numerical simulations. The findings also suggest that when storms pass over the boundary intersection zone in the PRD, relatively high possibility of rotating storm is expected even in a low-shear environment. Improved knowledge of such environments provides additional guidance to assess the regional tornado risk.



**Key words:** Tornado, mesovortex, surface boundary, land–sea contrast, monsoon

https://doi.org/10.1007/s00376-023-3095-5

# 1. Introduction

While tornadoes have been reported on every continent except Antarctica, their occurrences show a distinct diversity worldwide. Most tornadoes are found in the United States. According to the tornado records during 2010–2021 provided by the Storm Prediction Center, approximately 1200 tornadoes have struck the United States each year. The regional climate is demonstrated responsible for the large-scale environments that repeatedly encourage tornadic storms in that region (Brooks et al. 2003). Owing to the unstable low-level air from the Gulf of Mexico, the large lapse rate in the central United States and the regularly large vertical wind shear in spring contribute to the high tornado occurrence (Markowski and Richardson 2010).

Statistical studies have suggested that a broad spectrum of vertical wind shear and conditional instability combinations is capable of producing tornadoes. Significant severe thunderstorms that produce tornadoes are in general associated with high shear and high CAPE environments (Brooks et al. 2003). The ambient vertical wind shear is one of the important sources of low-level vertical vorticity within thunderstorms as a result of tilting and subsequent stretching of horizontal vorticity (Rotunno 1981; Rotunno and Klemp 1985; Davies-Jones 1984). Supercellular tornadoes have been demonstrated to preferentially form in high shear environments (Rotunno and Klemp 1985; Thompson et al. 2013; Anderson-Frey et al. 2019).

In the high shear region with large spatial coverage over the Great Plains, surface convergent boundaries such as drylines are often helpful to narrow the potential locations of severe thunderstorms and tornado development (Xue and Martin 2006a, b; Weckwerth and Parsons 2006). Some violent tornadoes are documented to be spawned by supercells that initiate along drylines, such as the EF5 Moore tornado in 2013 (e.g., Atkins et al. 2014; Burgess et al. 2014; Zhang et al. 2015). Along the entire length of dryline, typically hundreds of kilometers, the "triple point" (Reed and Albright 1997; Weiss and Bluestein 2002; Wakimoto et al. 2006) where three different airmasses intersect are more common locations for the initiation and intensification of tornadic supercells (e.g., the EF3 El Reno tornado; Wurman et al. 2014; Schumacher 2015). The preexisting enhanced vertical vorticity along boundaries or over the intersection zone by multiple boundaries could be a source of the initial vortex for stretching by large persistent and strong updrafts (e.g., Wakimoto and Wilson 1989; Houston and Wilhelmson 2007a, 2007b; Schenkman et al. 2012).

Although the preexisting ambient vertical vorticity is typically an order of magnitude smaller than the horizontal vorticity that is ultimately tilted in the vertical direction, the preexisting vertical vorticity seems to be important in the case of high-CAPE, low-shear tornadic events (Davies-Jones 2006; Houston and Wilhelmson 2012). More often, tornadoes that are associated with enhanced vertical vorticity (e.g., misocyclones) along boundaries result from non-mesocyclone processes, which typically are more difficult to forecast (Brady and Szoke 1989; Wakimoto and Wilson 1989; Lee and Wilhelmson 1997a, b, 2000). Statistical analyses have suggested that storms in low-shear environments are often unfavorable for supercellular organization and sometimes are quasi-linear convective systems (QLCSs) and disorganized cells or clusters (Thompson et al. 2003, 2012). Within these QLCSs, tornadoes and damaging straight-line winds are found to be closely associated with the embedded low-level meso-γ-scale vortex (i.e., mesovortex, 2–20 km in diameter; Orlanski 1975). These storms are characterized by a 0–6 km bulk wind shear magnitude of generally lower than 15 m $s^{-1}$ (Thompson et al. 2003). However, the presence of airmass boundaries may locally enhance the directional shear even in a large-scale low-shear environment, which sometimes alters the near-storm environment toward becoming more favorable for supercellular organization by a substantial increase in low-level shear.

In East Asia, the eastern China is also characterized by climatological tornado favorable conditions (Brooks et al. 2003). However, according to a recently compiled reliable database during the time period of 2007–2023, the tornado occurrences in China are only approximately 5% of those in the United States. The difference in regional climate results in the large discrepancy in tornado occurrences between the two countries (Zhou et al. 2021). As for the spatial distribution, tornadoes in China tend to be concentrated in coastal areas in eastern China, especially in Guangdong and Jiangsu provinces. Compared to the midlatitude counterparts in the United States, tornadoes in Guangdong Province are located closer to the tropics (Fig. 1a). Tornadoes in this region are overall weak (Fan and Yu 2015), which makes it even more challenging to detect and issue warnings. According to the statistics collected by the Foshan Tornado Research Center, the Pearl River Delta (PRD) has the highest tornado occurrences across Guangdong Province (Fig. 1a). The specific topography and regional climate in the PRD may have led to the relatively concentrated rather than a random distribution.



The coast of PRD is concave toward the sea, constituting a "trumpet" or "triangle" shape (Fig. 1b). After the onset of South China Sea summer monsoon that typically occurs in late May over the South China Sea (Wang and LinHo 2002), the prevailing low-level southwesterlies along with warm and moist air travel onshore (e.g., Chen et al. 2016; Du and Chen 2019; Bai et al. 2020), which often repeatedly produce baroclinic boundaries near coasts due to the land–sea contrast. When storms take place in the PRD region, these boundaries may interact with the storm-generated outflows forming new convergent boundaries. Comparing to the relatively random locations of drylines in the Great Plains, the locations of convergent boundaries that are associated with land–sea contrast are seemingly relatively fixed in this region. For years, forecasters have supposed that the trumpet-shaped PRD coastline may have played a role in the development of tornadic storms. The deployment of X-band phased array radars since 2019 in the PRD provides an opportunity to investigate the detailed formation process of tornadic storms with the aid of high temporal-spatial resolution sampling capacity. While the PRD is a climatological tornado hotspot in China, the annual tornado occurrences are still not very common and case studies would need to be conducted in order to better understand the formation and detection of tornadoes in this region.

The purpose of this two-part study is to explore the roles played by the trumpet-shaped coastline and its associated perturbed monsoonal flows in the formation of a tornadic storm in the PRD region. Part I primarily presents the mean state of low-level atmosphere due to the land–sea contrast, and the fine-scale evolutions of the focused storms, and the prestorm environments in the combined influence of the monsoon, land–sea contrast, storm outflows and unique topography. Part II complements the observational analysis and explores the detailed dynamics of mesovortex formation by convection-permitting numerical simulations. This storm developed in a low-shear environment where more often non-mesocyclone process is expected. Tornadic storms that initiate in low-shear flows are typically more difficult to forecast than those in high-shear environment. Understanding the formation processes of such tornadic storms may assist the refinement of methods used for tornado risk assessment in this region. The remainder of this paper is organized as follows. Section 2 presents the mean state of low-level atmosphere due to the land–sea contrast. The prestorm environments of the tornadic storm are provided in Section 3. Section 4 focuses on the observed analysis on the storms, gust fronts, and surface flows. Sections 5 and 6 presents the discussion and concluding remarks, respectively.



## 2. Coastal convergence associated with land–sea contrast

### *2.1 Design of numerical simulations*

To obtain the mean state of low-level atmosphere in the PRD region, a set of daily successive numerical simulations was conducted during three monsoon months using the

Advanced Research Weather Research and Forecasting (WRF-ARW) model (Skamarock et al. 2008), version 3.9.1. The WRF simulation was configured in one domain with a horizontal grid spacing of 4 km. The domain generally covers the area as shown in Fig. 1a. There were 50 terrain-following hydrostatic–pressure vertical levels topped at 50 hPa. The main parameterization configurations included the WRF single moment six-class (WSM6) microphysics (Hong et al., 2004), Yonsei State University (YSU) boundary-layer (Noh et al., 2003), revised MM5 Monin-Obukhov surface layer, thermal diffusion land surface, RRTM longwave radiation (Mlawer et al. 1997), and Dudhia shortwave radiation schemes. The cumulus parameterization scheme was turned off. The initial and lateral boundary conditions were provided by the fifth generation of ECMWF atmospheric reanalysis (ERA5) gridded data (horizontal resolution of 0.25°; hourly available; Hersbach et al. 2020). The model was initialized at 0000 UTC for a 30-h simulation on each day during June from 2019 to 2021. The first 6 h was regarded as the model spin-up time and thus the hourly output data for the last 24-h simulation were saved for analysis.

*2.2. Mean state of low-level atmosphere over the PRD during June*

Figure 2 presents the mean state of the thermodynamic and kinematic characteristics of near-ground atmosphere during June from 2019 to 2021. Distinct land–sea contrast in potential temperature at low levels was located over the PRD (Fig. 2a). In June when the South China Sea summer monsoon becomes active, this region typically is characterized by southwesterly moist air flows traveling onshore at low levels. When these large-scale monsoonal flows arrive on the PRD coasts, the prevailing low-level southwesterlies (refer to the red vector in Fig. 2a) tend to be horizontally sheared (refer to the blue vector in Fig. 2a) due to the land–sea contrast.

In the presence of the land–sea contrast of trumpet-shaped coastline, the downward branch of sea breeze circulation over the PRD water surface contributes to a tendency of easterly wind component on the west coasts. On the other hand, greater friction force is expected between the underlying surface and the bottom of the atmosphere on the land side. In the afternoon, the heated land strengthens the turbulent exchanges of momentum and thus also decelerates the lower-troposphere onshore flows on the coastal land. Consequently, negative tendency of $u$ component of the near-surface flow is expected in the west coastal area (Figs. 2b, c). The sheared onshore flows over the PRD water surface thus routinely produce a low-level convergence zone (refer to the dashed lines in Figs. 2b, c) along the west PRD coasts and a divergence zone over the water surface. In comparison to the relatively random locations of drylines in the Great Plains, the convergent boundary (refer to the ellipse in Fig. 2b) appears to be topography locked.

The fundamental fact is that the topography is fixed and the summer monsoon repeatedly occurs every year, indicative of a connection between the frequently occurred local severe weather and the unique topography and regional climate. Considering the relatively high frequency of tornado occurrence over the PRD region, the current study attempts to investigate the role of such an airmass boundary that is associated with the land–sea contrast in the regional tornadic storms. To reach that point, the first part of this study conducted a detailed observational analysis of a tornadic storm in this area. The tornadic case occurred during the monsoon active season in 2020 when multiple X-band phased-array weather radars have been deployed and operating in real time, which provides an opportunity to analyze the fine-scale storm structures at high temporal resolution.



## 3. Prestorm environment of the tornadic storm

### *3.1. Observational and model data*

For the purposes of synoptic and mesoscale analysis, observational data from surface weather stations, radiosondes and the ERA5 reanalysis gridded data were used. The densely deployed surface weather stations (gray dots in Fig. 1c) provide surface observations at an interval of 5 min. The nearby radiosonde (rhombus in Fig. 1c) and a wind profiling radar (square in Fig. 1c) were employed to obtain vertical profiles, including air temperature, moisture, and horizontal winds. The radiosonde was routinely launched twice a day and the profiles from wind profiling radar were available every 6 min with a vertical resolution of 100 m.

Two operational weather radars were used to depict the storm evolutions, including an S-band China New Generation Doppler Weather Radar (CINRAD) with dual-polarization capability (S-pol; green dot in Fig. 1c) and an X-band dual-polarization phased-array weather radar (X-PAR; red dot in Fig. 1c). The S-pol operated in the volume coverage pattern 21 (VCP21) mode during this event with a volumetric update time of approximately 6 min and a radial gate spacing of 250 m. The X-PAR was located approximately 6 km to the south of the reported tornado and operated an electronically scanned X-band planar antenna with dual polarization. A 360° volumetric update time was 90 s with 12 elevation angles (0.9°, 2.7°, 4.5°, 6.3°, 8.1°, 9.9°, 11.7°, 13.5°, 15.3°, 17.1°, 18.9°, and 20.7°). The radial gate spacing was 30 m and the azimuthal interval was 0.9° by adopting the oversampling techniques.



*3.2. Synoptic and mesoscale atmospheric conditions*

The tornadic storm of interest occurred in the early afternoon on 1 June 2020, after the onset of summer monsoon. It spawned a short-lived tornado (~7 min) at approximately 1250 BJT (Beijing time = UTC + 8 h) over the Pearl River estuary (Fig. 1b; Zhang et al. 2021). The lower troposphere was characterized by prevailing monsoonal southwesterlies in the coastal region of South China in the early morning, as indicated by upper-air observations (Fig. 3a, b).

A salient wind-shift line formed as the monsoonal southwesterlies converged with the subtropical westerlies (refer to the dashed curves in Fig. 3b). This synoptic forcing was responsible for the upstream mesoscale convective systems (MCSs) that were located to the west of Guangdong Province (labeled MCS-A in Fig. 4a). To the south of the wind-shift line, an 850-hPa jet stream was situated over the coastal land, leading to divergence on this level (refer to the dashed isopleth of 12 m $s^{-1}$ in Fig. 3b). Such a divergence combining the near-surface convergence due to the sea–land transition would produce a favorable dynamic structure for low-level upward motion and thus the formation of coastal storms (Du and Chen 2019).

At 1130 BJT, the PRD region was characterized by onshore southerlies near the surface (Fig. 3c). Under the influence of warm and humid tropical marine airmass advection, the region of interest had high thermodynamic instability with little convective inhibition. As revealed by the measurements of Hong Kong sounding taken in the early morning, the calculated surface-based CAPE (with virtual temperature correction), LCL and LFC were 3447 J $kg^{-1}$, 361 m and 554 m, respectively (Fig. 5a). These high-CAPE and low-LCL values are known to be conducive to the development of vigorous moist convection. Although the thermodynamic conditions were favorable for the formation of deep moist convection, the dynamic variables were generally not supportive of supercellular organization. Figure 5 shows that the horizontal wind speeds were overall light in the whole column of the troposphere. The 0–6 km bulk wind difference was only 7.2 m $s^{-1}$, which is small for the supercellular organization (Markowski and Richardson 2010). The 0–1 km storm relative helicity (SRH) was only 42 $m^2$ $s^{-2}$, which was calculated using the estimated storm-motion vector based on the method of Bunkers et al. (2000) for right-moving supercells. As shown in the hodograph diagram, the estimated storm motion (296°, 8.1 m $s^{-1}$) was toward the southeast (refer to the magenta vector in Fig. 5b). By tracking the radar echoes, the realistic storm motion (228°, 10.0 m $s^{-1}$) was toward a different direction (refer to the red vector in Fig. 5b). Using the realistic storm motion, the updated 0–1 km SRH value was reduced to only 7 $m^2 s^{-2}$, suggesting a low potential for cyclonic rotating updraft in right-moving supercells. Although dominated by unstable airmasses prior to the tornadogenesis, the region of interest was characterized by marginal values of supercell composite parameter (SCP) and significant tornado parameter (STP) due to the small SRH and bulk Richardson number (BRN) shear (Thompson et al. 2003).

Figure 6 presents the evolution of wind profiles under the precipitation-free conditions obtained from the wind-profiling radar located approximately 15 km to the south of the tornado location (Fig. 1c). Consistent with the earlier sounding observations, the wind profiles derived from wind-profiling radar suggested that the lowest 500 m layer was generally characterized by southerlies and the upper layer by southwesterlies. Approximately one hour before tornadogenesis, the 1.5–2 km AGL layer underwent an enhancement of wind speed. The wind directions from the near-surface to 2 km AGL became more veering with height. Although the directional and speed shears between surface and upper layers have increased before tornadogenesis, the integrated index of 0–1 km SRH was overall small, with a value generally less than 20 $m^2 s^{-2}$. On the other hand, the speed enhancement near the top of PBL may have enhanced the vertical momentum transport at lower levels, priming the mesoscale environment for convective initiation and development.

The above analyses suggest that the tornadic storm formed in the destabilized atmosphere ahead of a synoptic wind-shift line but in a low-shear environment. Although the high conditional instability supports convective development, the dynamic conditions suggest that this environment was marginally favorable for the expected supercellular storm type as indicated by the low values of vertical wind shear. The marginal STP values also suggest a very low potential for supercellular tornado in the region of interest.

## 4. Observational analysis on the storms, gust fronts and monsoonal flows

*4.1. Storm evolutions obtained from radar observations*

The tornadic storm was embedded in the southern-end part of a quasi-linear convective system (QLCS, Fig. 4b). It initiated at approximately 1218 BJT (refer to Storm S2 in Fig. 7b) as part of multiple scattered convective cells that were aligned in a southwest–northeast orientation (refer to the dashed rectangle in Fig. 7a). The storm propagated toward northeast and its northern part merged with a preexisting Storm S3 at 1236 BJT (Fig. 7c). During the period from 1248 to 1254 BJT, a southern storm labeled S1 caught up and merged with the southern part of tornadic Storm S2 (Fig. 7d, e). A “hook” echo signature was identified between Storms S1 and S2 at the lowest radar level at 1254 BJT (refer to the notch of reflectivity labeled Hook in Fig. 4b). The reported tornado was located slightly to the south of this hook echo. The subsequent X-PAR analysis in the following subsection provides more details on the fine-scale storm structures.

In the S-Pol volume scan when the tornadic storm initiated, a radar fine line was identified at the 0.5° elevation angle (Fig. 7f). It was located approximately 7 km to the west of Storm S2. The surface observations from two surface weather stations (labeled A and B in Fig. 7f) confirmed that this radar fine line was the leading edge of storm cold outflows (i.e., gust front). These two stations were almost located on the radar fine line at 1218 BJT. At Station A, a sharp decrease in surface temperature (4°C) and a slight pressure jump were observed from 1220 to 1225 BJT (Fig. 8a). Meanwhile, the surface winds turned westerly from southwesterly and intensified to 15.1 m s$^{-1}$ from 8.2 m s$^{-1}$. The relative humidity also underwent an evident increase from 72% to 85% within 10 min. To the south of this station, Station B observed rapid changes in surface temperature, wind, humidity and pressure from approximately 1215 BJT

(Fig. 8b). The confirmed gust front moved eastward and caught up with the tornadic storm at 1236 BJT when this storm merged with its northern Storm S3 (Fig. 7c).

The merging process was more clearly observed by X-PAR at a finer spatiotemporal resolution (Fig. 9). Prior to the hook echoes, a "finger-like" echo signature started to be identified by X-PAR from 1235:30 BJT, and this signature was even more pronounced after 1240:00 BJT. Note that the S-Pol observations have suggested that the contact between the aforementioned gust front and the tornadic Storm S2 occurred nearly at that time (Fig. 7c) while the precise location of gust front was difficult to confirm because of the interference of precipitation echoes. The station surface winds valid at 1235 BJT indeed suggest that the gust front was in proximity to the tornadic storm at that time. The X-PAR radial velocity at the lowest radar level shows that the southwestern edge of Storm S2 underwent a transition from outbound to inbound radial velocity from 1231:00 to 1235:30 BJT (Fig. 10). As shown in Fig. 10a, the distance between Station A and the western edge of Storm S2 was approximately 9 km and thus the average translation speed of the radar fine line was simply estimated as 8.8 m $s^{-1}$ during 1218–1235 BJT. At Station C (Fig. 10a), during the passage of surface cold outflows, the observed wind speed was 9.6 m $s^{-1}$ at 1235 BJT. Considering the deformation of the density current, it seems reasonable to presume that the gust front almost had interacted with Storm S2 at 1235 BJT, after which the finger-like echo signature developed.

From 1245:00 to 1249:30 BJT, there was an indication of reflectivity wrap-up, indicative of strong midlevel cyclonic rotations (Fig. 9c, d). At the 8.1° elevation angle, a well-defined meso-γ-scale cyclonic signature was identified near the tip of the finger-like echoes (Fig. 9e, f). While the radar-based structures of the tornadic storm present a supercellular organization, the storm is believed to be a non-mesocyclone process because a closer inspection shows that the mesocyclonic rotation originated from low levels and shallow in depth. Here the meso-γ-scale cyclonic signature in the Doppler products represents a mesovortex. The mesovortex formed before the merger of Storms S1 and S2 (Fig. 9c–f). The maximum height of the measurable mesocyclonic signatures in all volume scans was approximately 4 km AGL. The distance of the maxima of the couplet signature in the radial velocity field ranged from 2 to 3 km (e.g., Figs. 9f and 11). In this study, the detailed quantitative evolution of the mesovortex structure is not presented because the velocity couplet features were sometimes incomplete due to the relatively low detection sensitivity of X-PAR. For example, the maxima in the outbound part of the velocity couplet signature in Fig.9e was not measurable. Compared to the typical supercells in the U.S. Great Plains, the current supercell-like storm was miniature. The fine structure of this hook echo signature was difficult to identify by the operational S-Pol radar (e.g., Figs. 4b).

Beneath the mesovortex, a weak tornadic vortex signature (TVS) was identified at the 0.9° elevation angle at 1251:00 BJT when the northern part of Storm S1 had started to merge with the hook echoes of Storm S2 (Fig. 12a, b). Meanwhile, a relatively weak-echo "hole" signature was identified around the TVS (Fig. 12a–d). In the fields of the co-polar cross-correlation coefficient ($\rho_{HV}$) products, a localized area of small-value $\rho_{HV}$ was identified near the TVS (inset in Fig. 12b). Low $\rho_{HV}$ was often associated with lofted tornadic debris, which typically had random orientations and irregular shapes and thus resulted in a low $\rho_{HV}$ signature. In the following volume scan, the maximum gate-to-gate radial velocity difference of the 0.9° TVS was 19 m s$^{-1}$ with anomalously low $\rho_{HV}$ less than 0.6 (Fig. 12f). During the tornadic event, the diameter of the low-$\rho_{HV}$ area was generally less than 400 m (insets in Fig. 12e–h). The TVS intensity peaked at 1254:00 BJT with a maximum gate-to-gate radial velocity difference of 22 m s$^{-1}$ at 420 m AGL (Fig. 12g). The TVS lost its clear identification after 1257:00 BJT. The reflectivity fields from X-PAR also demonstrate that the tornado formed at the tip of hook echo

(Figs. 12 a–d). Comparing to the S-Pol observations (Fig. 4b), Fig. 12c appears two notches along the hook echo due to the merging process.

*4.2. Collocation between the storm, gust front, and monsoonal flows*

The aforementioned radar and surface observations provide evidence of the juxtaposition of finger-like echoes and the surface triple point. Figure 9a shows that before the formation of finger-like echoes, the southern part of Storm S2 was located at the triple point formed by the eastward-moving outflows and southwesterly and southeasterly flows (refer to the black, red and magenta curved arrows, respectively). After the gust front having arrived at the triple point at approximately 1236 BJT, the finger-like echoes developed and subsequently produced a low-level mesovortex in the following 5 min (e.g., Fig. 9b, e). The close proximity in time and space of the mesovortex to the surface triple point might have contributed to the generation of mesovortex. Previous studies have suggested that the enhanced low-level vertical vorticity along convergent boundaries sometimes directly promotes the formation of mesocyclone or mesovortex and that longer-lived, strong low-level updrafts on these boundaries are more likely to support midlevel rotations (e.g., Houston and Wilhelmson 2007b). The current surface analysis based on surface weather stations suggests that the triple point where three different airmasses intersect was a source to provide preexisting ambient vertical vorticity at low levels. The subsequent forced lifting associated with gust front would further enhance the upward motions over the triple-point zone and thus intensify the stretching of the locally enhanced low-level vertical vorticity in that region. Based on the observational evidence, the fact is that the finger-like echoes and subsequent mesovortex formed when the gust front was intruding into the triple point zone. By conducting multiple sensitivity numerical simulations in Part II of this study, it is demonstrated that the triple point due to the trumpet-shaped coastline (through a sensitivity experiment by modifying the coastline shape) and the intruding gust front (through a sensitivity experiment by strengthening cold pools) both have played an important role in the formation of low-level mesovortex in this case.

In addition to the potentially important roles of triple point and gust front in the mesovortex generation, it is still not clear that whether the merger between Storm S1 and the tornadic storm S2 (Figs. 9c, d) has contributed to the intensification of the existing mesovortex (Fig. 11). Flournoy et al. (2022) documented that storm merging processes are quite common in supercell events. Although no general relationship is found between storm merger and temporal changes in low-level mesocyclone strengths, qualitative results yield after thresholding the outcome of merger events on the mesocyclone strength before merger. Their statistics suggest that the initially weak mesocyclones are more likely to intensify after storm mergers while the initially strong mesocyclones are more likely to weaken. In the current case, the weak mesovortex has formed before the merger between Storm S1 and the hook echoes (e.g., Fig. 11d–f). It is a fact that the mesovortex intensified and then produced a tornado shortly after the merger event (Figs. 9 and 12). Although it is hard to demonstrate the exact role of merger process in the mesovortex intensification and tornadogenesis, the cold pool outflows emanated from the approaching Storm S1 could have locally altered the near-storm-scale environments around the low-level mesovortex. During this case, multiple merger events have occurred in the southern-end part of the QLCS. After the demise of the short-lived tornado, two storms (labeled S3 and S4 in Fig. 4b) to the south of the hook echoes caught up and merged with the hook echoes. Over the triple point, another supercell-like structure (labeled Hook echo B in Figs. 13a, b) in rain field formed in southern-end part of Storm S4. The radial velocity fields appeared a mesocyclonic signature at the low radar levels but this meso-γ-scale vortex was overall weak and short-lived (Figs. 13c, d).

# 5. Discussion

During the active season of South China Sea summer monsoon, the PRD area is significantly influenced by onshore southwesterlies in the lower troposphere. The onshore monsoonal flows present a salient feature of horizontal heterogeneity over the estuary of the Pearl River due to the land–sea contrast of the trumpet-shaped coastline (Fig. 14a). This unique land–sea contrast leads to a routinely formed convergent boundary on the west coast in the influence of the warm southwesterlies on land and the sheared monsoonal flows with relatively cool airmasses from the PRD water surface. Chen et al. (2016) conducted a radar climatology and a set of sensitivity numerical simulations to investigate the characteristics of land–sea breezes and the related rainfall in this region. Results suggest that convective rainfall is primarily located on the west coast of PRD. After removing the inhomogeneity of coastline (no trumpet shape), the semi-ideal numerical simulations show a significantly different regional pattern of coastal convection in this area. These findings support the potential influence of the convergent boundary due to the trumpet-shaped coastline on the regional convective weather.

When cold pools emanated from the northern storms block the onshore flows, three airmass boundaries are present, producing a triple point near the Pearl River estuary, as in this case (Fig. 14). The local maxima in vertical vorticity (e.g., misocyclones) along convergent boundaries that originate from horizontal shearing instability (Kingsmill 1995) increase the risks of rotating storms even in the dynamic conditions that are unfavorable for supercellular organization. In contrast with the along-boundary heterogeneity, the triple point caused by boundary intersections is also believed to create risk for an upcoming storm to organize into a rotating storm because of the preexisting vertical vorticity in that region. Such a possibility would be even higher when storms successively propagate toward and pass over a triple point. On the other hand, because the position of triple point is relatively slow-moving or fixed, a subsequent mismatch regarding the position between the triple point and mesovortex that propagates along with storms tends to be unfavorable for a strong midlevel rotation.

It should be noted that the PRD is a hotspot of thunderstorm (Zhang et al. 2017; Bai et al. 2020) while tornadic storms are still rare events over the estuary of Pearl River where the triple point often forms. The fact suggests that even though the unique topography provides favorable conditions for a higher probability of rotating storms comparing to the neighboring coasts of southern China, smaller storm-scale processes beyond the mesoscale environment may eventually determine the tornadogenesis. On the other hand, it is difficult to detect the vertically oriented vortices and estimate their strengths by Doppler weather radars. Previous studies have documented that some radars that incorporate high power transmitters have the capability to detect misocyclones (with weak ambient vertical vorticity) aligned with airmass boundaries, such as the mobile Doppler radars during the International H2O Project (Wurman et al. 1997; Marquis et al. 2007). In the PRD region, dozens of polarimetric X-PARs have been deployed in last two years while they are characterized by relatively low detection sensitivity due to the limited peak transmitted power (~400 W), which makes it hard to detect these vortices in the precipitation-free condition. Owing to the densely deployed surface weather stations in this region, a qualitative recognition could be achieved based on the horizontal winds measured by these stations. The assessment combining the surface observations and storm evolutions from radar products may still provide guidance to assess the severe weather over the triple point zone.

## 6. Concluding remarks

This article examined the prestorm environment and the structures and evolutions of a tornadic storm in the vicinity of a triple point where three different airmasses intersected on the irregular coasts of southern China during the summer monsoon season in 2020. Analysis was carried out primarily using a rapid scan X-band phased-array radar (X-PAR) that was located only 6 km from the storm of interest, an S-band operational radar (S-Pol), and surface weather stations. Comparing to the S-Pol, the X-PAR presents more supercell-like features, such as mesocyclonic structures, notches and hook echoes in the velocity and reflectivity products.

The tornadic storm occurred in a high-CAPE but low-shear environment when the South China Sea summer monsoon was active. Over the estuary of Pearl River, surface cold outflows that were generated by preexisting storms separately produced convergent boundaries with the southwesterly and southeasterly flows (Fig. 14a). The three types of airmasses converged and contributed to an enhanced convergent zone over the boundary intersection point (triple point). As a cold surge of westerly momentum at low levels approached this zone, finger-like pendant echoes formed (Fig. 14a). A subsequent reflectivity wrap-up process leading to hook echoes was identified over the triple point, indicating a strong low-to-middle level rotation in that region (Fig. 14b). The lowest tornadic vortex signature detected by the X-PAR appeared shortly after a convective cell merged with the hook echoes.



The storm-boundary interaction under the influence of the monsoon, land–sea contrast, storm outflows, and the unique regional topography may be an important contribution to rotating storms (and even tornadoes) over the PRD. The authors have identified several tornadic storms that are similar to the current case in this region. While the observational analysis provides some insights into the role of trumpet-shaped coastline in regard to the 1 June 2020 PRD tornadic event, a number of questions remain unanswered, such as the number of tornadoes that are associated with the similar dynamics. The dependence of the mesovortex predictability on the degree of the representation of coastline fine structures in NWP models, especially in a low-shear environment, is also an interesting topic. As documented above, this study is novel in the sense that it documents a tornado event that is associated with the trumpet-shaped coastline. The unique land–sea contrast connects the severe weather and the regional climate, which may provide additional guidance to assess tornado risk in this region. In the second article (Part II) of this series, a set of numerical simulations are conducted to investigate the mesovortex genesis as discussed in the observational analysis.

***Acknowledgments.*** This study was supported by the National Natural Science Foundation of China (Grants 42275006, U2242203 and 42030604) and the Guangdong Basic and Applied Basic Research Foundation (Grant 2023A1515011705). The reanalysis data used for this article can be accessed on the European Centre for Medium-Range Weather Forecasts (ECMWF) website (https://cds.climate.copernicus.eu/cdsapp#!/dataset/reanalysis-era5-pressure-levels?tab=form) and the radar and surface observations are provided by the Guangzhou Meteorological Observatory. The authors are grateful for the helpful reviews provided by the editors and anonymous reviewers.



## REFERENCES

Anderson-Frey, A. K., Y. P. Richardson, A. R. Dean, R. L. Thompson, and B. T. Smith, 2019: Characteristics of Tornado Events and Warnings in the Southeastern United States. *Wea. Forecasting*, **34**, 1017–1034. https://doi.org/10.1175/WAF-D-18-0211.1

Atkins, N. T., K. M. Butler, K. R. Flynn, and R. M. Wakimoto, 2014: An Integrated Damage, Visual, and Radar Analysis of the 2013 Moore, Oklahoma, EF5 Tornado. *Bull. Amer. Meteor. Soc.*, **95**, 1549–1561. https://doi.org/10.1175/BAMS-D-14-00033.1

Bai, L., G. Chen, and L. Huang, 2020: Convection Initiation in Monsoon Coastal Areas (South China). Geophysical Research Letters, 47, e2020GL087035. https://doi.org/10.1029/2020GL087035

Bai, L., Z. Meng, K. Sueki, G. Chen, and R. Zhou, 2020: Climatology of tropical cyclone tornadoes in China from 2006 to 2018. *Science China Earth Sciences*, **63**, 37–51. https://doi.org/10.1007/s11430-019-9391-1

Brady, R.H., and E.J. Szoke, 1989: A case study of nonmesocyclone tornado development in northeast Colorado: similarities to waterspout formation. *Mon. Wea. Rev.*, **117**, 843–856. https://doi.org/10.1175/1520-0493(1989)117<0843:ACSONT>2.0.CO;2

Brooks, H. E., J. W. Lee, and J. P. Craven, 2003: The spatial distribution of severe thunderstorm and tornado environments from global reanalysis data. *Atmos. Res.*, **67-68**, 73–94. https://doi.org/10.1016/S0169-8095(03)00045-0

Bunkers, M. J., B. A. Klimowski, J. W. Zeitler, R. L. Thompson, and M. L. Weisman, 2000: Predicting Supercell Motion Using a New Hodograph Technique. *Wea. Forecasting*, **15**, 61–79. https://doi.org/10.1175/1520-0434(2000)015<0061:PSMUAN>2.0.CO;2

Burgess, D., and Coauthors, 2014: 20 May 2013 Moore, Oklahoma, Tornado: Damage Survey and Analysis. *Wea. Forecasting*, **29**, 1229–1237. https://doi.org/10.1175/WAF-D-14-00039.1

Chen, X., F. Zhang, and K. Zhao, 2016: Diurnal Variations of the Land–Sea Breeze and Its Related Precipitation over South China. Journal of the Atmospheric Sciences, 73, 4793–4815. https://doi.org/10.1175/JAS-D-16-0106.1

Du, Y., and G. Chen, 2019: Climatology of Low-Level Jets and Their Impact on Rainfall over Southern China during the Early-Summer Rainy Season. Journal of Climate, 32, 8813–8833. https://doi.org/10.1175/JCLI-D-19-0306.1

Davies-Jones, R. P., 1984. Streamwise vorticity: the origin of updraft rotation in supercell storms. *J. Atmos. Sci.,* **41**, 2991–3006. https://doi.org/10.1175/1520-0469(1984)041<2991:SVTOOU>2.0.CO;2

Davies-Jones, R. P., H. E. Brooks, 1993. Mesocyclogenesis from a theoretical perspective. Tornadoes and tornadic storms: a review of conceptual models. The Tornado: Its Structure, Dynamics, Prediction, and Hazards. *Geophys. Monogr. Amer. Geophys*. Union, pp. 105–114. No. 79.

Davies-Jones, R., 2006: Tornadogenesis in supercell storms: What we know and what we don't know. Preprints, Symp. on the Challenges of Severe Convective Storms, Atlanta, GA, *Amer. Meteor. Soc.*, 2.2.

Du, Y., and G. Chen, 2019: Heavy Rainfall Associated with Double Low-Level Jets over Southern China. Part II: Convection Initiation. *Mon. Wea. Rev.*, **147**, 543–565. https://doi.org/10.1175/MWR-D-18-0102.1

Fan, W. and Yu, X., 2015: Characteristics of spatial-temporal distribution of tornadoes in China (in Chinese with English abstract). *Meteor. Mon.*, **41**, 793–805.

Flournoy, M. D., A. W. Lyza, M. A. Satrio, M. R. Diedrichsen, M. C. Coniglio, and S. Waugh, 2022: A Climatology of Cell Mergers with Supercells and Their Association with Mesocyclone Evolution. *Mon. Wea. Rev.*, 150, 451–461.

Hersbach, H., and Coauthors, 2020: The ERA5 global reanalysis. Quart. J. of the Royal Meteorological Society, 146, 1999–2049. https://doi.org/10.1002/qj.3803

Houston, A. L., and R. B. Wilhelmson, 2007a: Observational Analysis of the 27 May 1997 Central Texas Tornadic Event. Part I: Prestorm Environment and Storm

Maintenance/Propagation. *Mon. Wea. Rev.*, **135**, 701–726. https://doi.org/10.1175/MWR3300.1

Houston, A. L., and R. B. Wilhelmson, 2007b: Observational Analysis of the 27 May 1997 Central Texas Tornadic Event. Part II: Tornadoes. *Mon. Wea. Rev.*, **135**, 727–735. https://doi.org/10.1175/MWR3301.1

Houston, A. L., and R. B. Wilhelmson, 2012: The Impact of Airmass Boundaries on the Propagation of Deep Convection: A Modeling-Based Study in a High-CAPE, Low-Shear Environment. *Mon. Wea. Rev.*, **140**, 167–183. https://doi.org/10.1175/MWR-D-10-05033.1

Kingsmill, D. E., 1995: Convection Initiation Associated with a Sea-Breeze Front, a Gust Front, and Their Collision. *Mon. Wea. Rev.*, 123, 2913–2933. https://doi.org/10.1175/1520-0493(1995)123<2913:CIAWAS>2.0.CO;2

Lee, B. D., and R. Wilhelmson, 1997a: The numerical simulation of nonsupercell tornadogenesis. Part I: Initiation and evolution of pretornadic misocyclone circulations along a dry outflow boundary. *J. Atmos. Sci.*, **54**, 32–60, https://doi.org/10.1175/1520-0469(1997)054<0032:TNSONS>2.0.CO;2

Lee, B. D., and R. Wilhelmson, 1997b: The numerical simulation of nonsupercell tornadogenesis. Part II: Evolution of a family of tornadoes along a weak outflow boundary. *J. Atmos. Sci.*, **54**, 2387–2414, https://doi.org/10.1175/1520-0469(1997)054<2387:TNSONT>2.0.CO;2

Lee, B. D., and R. Wilhelmson, 2000: The numerical simulation of nonsupercell tornadogenesis. Part III: Tests investigating the role of CAPE, vortex sheet strength, and boundary layer vertical shear. *J. Atmos. Sci.*, **57**, 2246–2261, https://doi.org/10.1175/1520-0469(2000)057<2246:TNSONT>2.0.CO;2

Markowsk, P., and Y. Richardson, 2010: Mesoscale Meteorology in Midlatitudes. Wiley-Blackwell, 407 pp.

Markowsk, P., and Y. Richardson, 2009: Tornadogenesis: Our current understanding, forecasting considerations, and questions to guide future research. *Atmos. Res.*, **93**, 3–10. https://doi.org/10.1016/j.atmosres.2008.09.015

Markowski, P., Y. Richardson, and G. Bryan, 2014: The Origins of Vortex Sheets in a Simulated Supercell Thunderstorm. *Mon. Wea. Rev.*, **142**, 3944–3954. https://doi.org/10.1175/MWR-D-14-00162.1

Marquis, J. N., Y. P. Richardson, and J. M. Wurman, 2007: Kinematic Observations of Misocyclones along Boundaries during IHOP. *Mon. Wea. Rev.*, 135, 1749–1768.

Mlawer, E. J., S. J. Taubman, P. D. Brown, M. J. Iacono, and S. A. Clough, 1997: Radiative transfer for inhomogeneous atmospheres: RRTM, a validated correlated-k model for the longwave. J. Geophys. Res., 102, 16663–16682. https://doi.org/10.1029/97JD00237

Noh, Y., W. Cheon, S. Hong, and S. Raasch, 2003: Improvement of the K-profile model for the planetary boundary layer based on large eddy simulation data. Boundary-Layer Meteor., 107, 401–427. https://doi.org/10.1023/A:1022146015946

Orlanski, I., 1975. A rational subdivision of scales for atmospheric processes. Bull. Am. Meteorol. Soc. 56, 527–530.

Reed, R. J., and M. D. Albright, 1997: Frontal structure in the interior of an intense mature ocean cyclone. *Wea. Forecasting*, 12, 866–876.

Rotunno, R., 1981: On the Evolution of Thunderstorm Rotation. *Mon. Wea. Rev.*, **109**, 577–586. https://doi.org/10.1175/1520-0493(1981)109<0577:OTEOTR>2.0.CO;2

Rotunno, R., and J. Klemp, 1985: On the Rotation and Propagation of Simulated Supercell Thunderstorms. *J. Atmos. Sci.*, **42**, 271–292. https://doi.org/10.1175/1520-0469(1985)042<0271:OTRAPO>2.0.CO;2

Schenkman, A. D., M. Xue, and A. Shapiro, 2012: Tornadogenesis in a Simulated Mesovortex within a Mesoscale Convective System. *J. Atmos. Sci.*, **69**, 3372–3390. https://doi.org/10.1175/JAS-D-12-038.1

Schenkman, A. D., M. Xue, and M. Hu, 2014: Tornadogenesis in a High-Resolution Simulation of the 8 May 2003 Oklahoma City Supercell. *J. Atmos. Sci.*, **71**, 130–154. https://doi.org/10.1175/JAS-D-13-073.1

Schumacher, R. S., 2015: Resolution dependence of initiation and upscale growth of deep convection in convection-allowing forecasts of the 31 May–1 June 2013 supercell and MCS. *Mon. Wea. Rev*, **143**, 4331–4354. https://doi.org/10.1175/MWR-D-15-0179.1

Skamarock, W. C., and Coauthors, 2008: A description of the Advanced Research WRF version 3. NCAR Tech. Note NCAR/TN-475+STR, 113 pp. [Available online at http://www.mmm.ucar.edu/wrf/users/docs/arw_v3_bw.pdf.]

Thompson, R. L., B. T. Smith, A. R. Dean, and P. T. Marsh, 2013: Spatial distributions of tornadic near-storm environments by convective mode. Electronic *J. Severe Storms Meteor.*, **8**, 1–22.

Thompson, R. L., B. T. Smith, J. S. Grams, A. R. Dean, and C. Broyles, 2012: Convective Modes for Significant Severe Thunderstorms in the Contiguous United States. Part II: Supercell and QLCS Tornado Environments. *Wea. Forecasting*, **27**, 1136–1154. https://doi.org/10.1175/WAF-D-11-00116.1

Thompson, R. L., R. Edwards, J. A. Hart, K. L. Elmore, and P. Markowski, 2003: Close Proximity Soundings within Supercell Environments Obtained from the Rapid Update Cycle. *Wea. Forecasting*, **18**, 1243–1261. https://doi.org/10.1175/1520-0434(2003)018<1243:CPSWSE>2.0.CO;2

Wakimoto, R. M., and J. W. Wilson, 1989: Non-supercell Tornadoes. *Mon. Wea. Rev.*, **117**, 1113–1140. https://doi.org/10.1175/1520-0493(1989)117<1113:NST>2.0.CO;2

Wakimoto, R. M., H. V. Murphey, E. V. Browell, and S. Ismail, 2006: The “Triple Point” on 24 May 2002 during IHOP. Part I: Airborne Doppler and LASE Analyses of the Frontal Boundaries and Convection Initiation. *Monthly Weather Review*, 134, 231–250.

Wang, B., and LinHo, 2002: Rainy Season of the Asian–Pacific Summer Monsoon. *J. Climate*, **15**, 386–398. https://doi.org/10.1175/1520-0442(2002)015<0386:RSOTAP>2.0.CO;2

Weiss, C. C., and H. B. Bluestein, 2002: Airborne pseudo-dual Doppler analysis of a dryline-outflow boundary intersection. *Monthly Weather Review*, 130, 1207–1226.

Weckwerth, T. M., and D. B. Parsons, 2006: A Review of Convection Initiation and Motivation for IHOP_2002. *Monthly Weather Review*, 134, 5–22. https://doi.org/10.1175/MWR3067.1

Wurman, J., J. Straka, E. Rasmussen, M. Randall, and A. Zahrai, 1997: Design and Deployment of a Portable, Pencil-Beam, Pulsed, 3-cm Doppler Radar. *Journal of Atmospheric and Oceanic Technology*, 14, 1502–1512.

Wurman, J., K. Kosiba, P. Robinson, and T. Marshall, 2014: The Role of Multiple-Vortex Tornado Structure in Causing Storm Researcher Fatalities. *Bull. Amer. Meteor. Soc.*, **95**, 31–45. https://doi.org/10.1175/BAMS-D-13-00221.1

Xue, M., and W. J. Martin, 2006a: A High-Resolution Modeling Study of the 24 May 2002 Dryline Case during IHOP. Part I: Numerical Simulation and General Evolution of the Dryline and Convection. *Monthly Weather Review*, 134, 149–171. https://doi.org/10.1175/MWR3071.1

Xue, M., and W. J. Martin, 2006b: A High-Resolution Modeling Study of the 24 May 2002 Dryline Case during IHOP. Part II: Horizontal Convective Rolls and Convective Initiation. *Monthly Weather Review*, 134, 172–191. https://doi.org/10.1175/MWR3072.1

Zhang, Y., F. Zhang, D. J. Stensrud, and Z. Meng, 2015: Practical Predictability of the 20 May 2013 Tornadic Thunderstorm Event in Oklahoma: Sensitivity to Synoptic Timing and Topographical Influence. *Mon. Wea. Rev.*, **143**, 2973–2997. https://doi.org/10.1175/MWR-D-14-00394.1

Zhang, Y., L. Bai, Z. Meng, B. Chen, C. Tian, and P. Fu, 2021: Rapid-scan and polarimetric phased-array radar observations of a tornado in the Pearl River Estuary. *J. of Tropical Meteor.*, **27**, 80–85. https://doi.org/10.46267/j.1006-8775.2021.008

Zhou, R., Z. Meng, and L. Bai, 2021: Differences in Tornado Activities and Key Tornadic Environments between China and the United States. *International J. Climatology*, **42**, 1–18. https://doi.org/10.1002/joc.7248

Zhou, R., Z. Meng, and L. Bai, 2020: Tornado Database in China (2007~2016), Peking University Open Research Data Platform. https://doi.org/10.18170/DVN/QKQHTG

## FIGURES

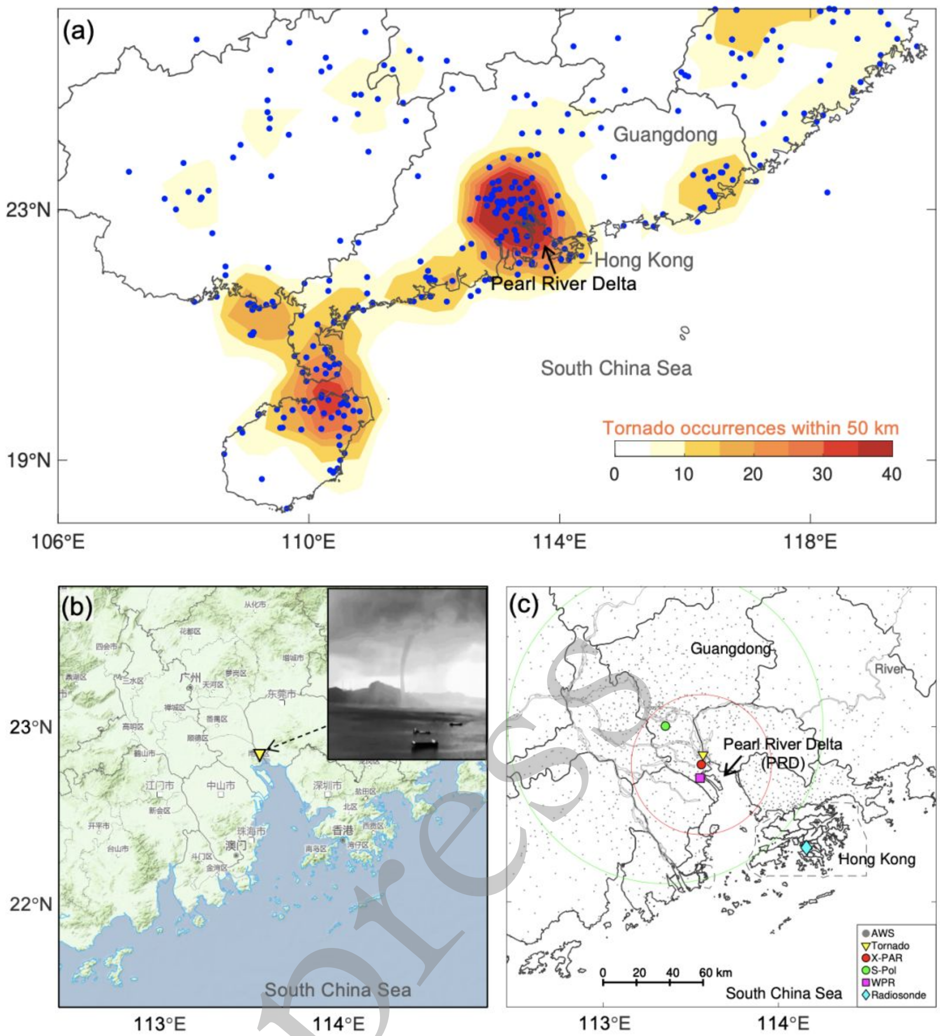




**Fig. 1.** (a) Tornado locations (blue dots) over the period from 2007 to 2022. The shadings denote the numbers of tornado occurrence within a range of 50 km. These tornado records are provided by Peking University (Zhou et al. 2020, 2021) and the Foshan Tornado Research Center. (b) Snapshot of the Satellite image around the Pearl River Delta. The yellow triangle represents the rough location of the tornado as shown in the inset panel. (c) The observational platforms used for analysis in this study. The locations of the tornado, X-band phased-array radar (X-PAR), S-band operational radar (S-Pol), wind-profiler (WPR) radar, radiosonde, and automated weather station (AWS) are denoted by triangle, red dot, green dot, square, rhombus, and gray dot, respectively.

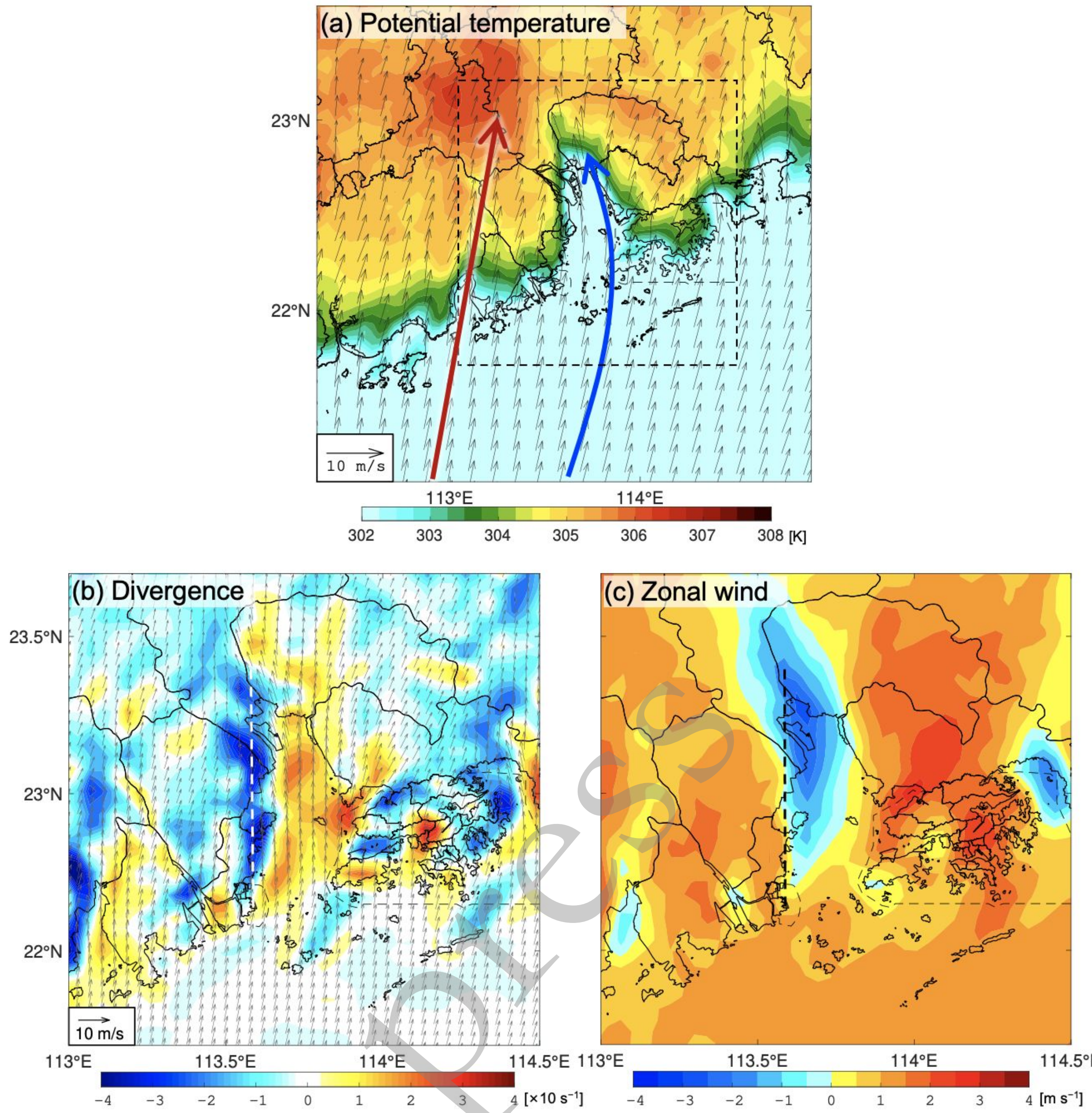


**Fig. 2.** (a) Average potential temperature (shaded) and horizontal winds (vectors) on the WRF model level 1 above the ground valid at 1500 BJT in June from 2019 to 2021. The red arrow represents the low-level prevailing onshore flows and the blue curved arrow represents the sheared onshore flows due to the land–sea contrast. (b) Same as (a) but for the average convergence (cool color) and divergence (warm color) enlarged in the rectangle in (a). (c) Average zonal components of horizontal winds on the WRF model level 1 above the ground valid at 1500 BJT in June from 2019 to 2021. The dashed lines denote the convergent boundaries on the west coasts of the Pearl River Delta.

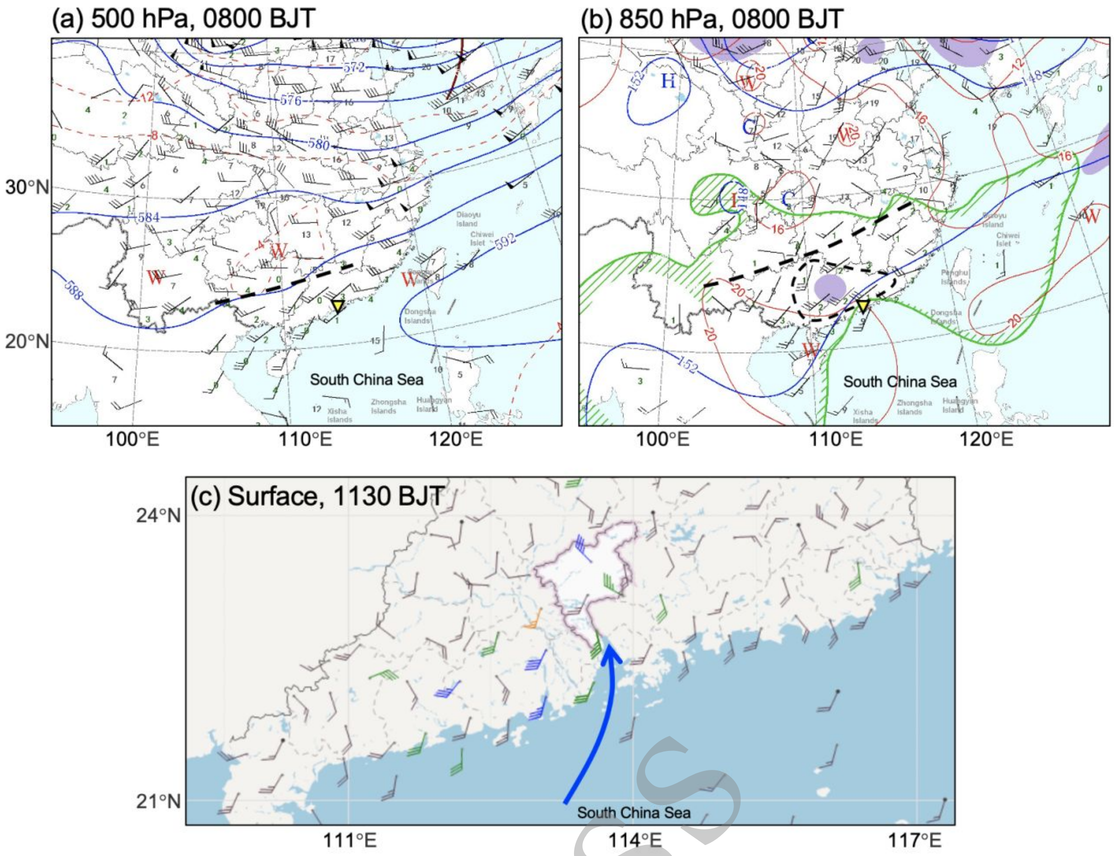


**Fig. 3.** Observed synoptic analysis on (a) 500 hPa, (b) 850 hPa and (c) surface levels on 1 June 2020. The background weather maps in (a),(b) and (c) are originally produced by the National Meteorological Center and Guangzhou Meteorological Observatory, respectively. The tornado location is marked by yellow triangle. The half barbs, full barbs, and pennants denote 2, 4, and 20 m $s^{-1}$, respectively. In (a), geopotential heights (units: dagpm), temperature (units: degree C), and wind shift line are represented by blue, red, and dashed black curves, respectively. In (b), the dashed isopleth represents the area with a wind speed greater than 12 m $s^{-1}$ on 850 hPa. The green isopleths mark the boundaries with a mixing ratio of 12 and 15 g $kg^{-1}$, respectively. The moist side is rasterized.

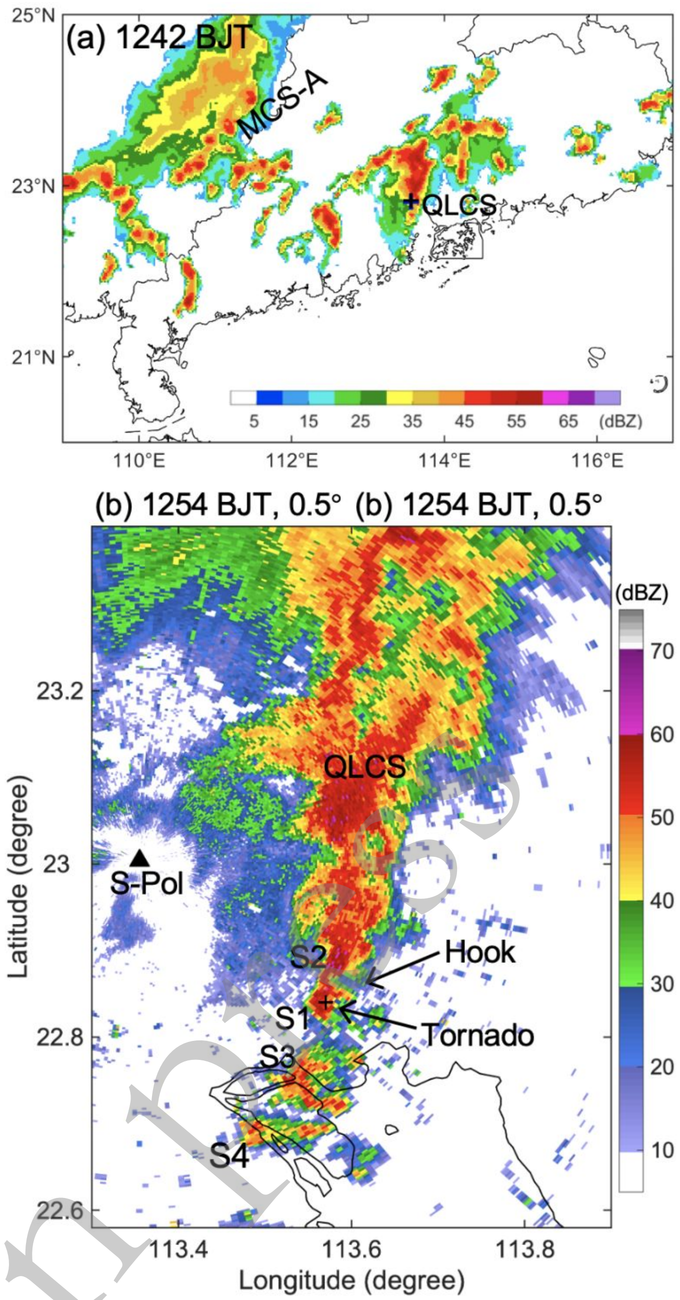


**Fig. 4.** (a) Composite radar reflectivity at 1242 BJT on 1 June 2020. (b) Radar reflectivity at the 0.5° elevation angle from the S-band operational radar at 1254 BJT on 1 June 2020. The black crosses mark the approximate tornado locations.

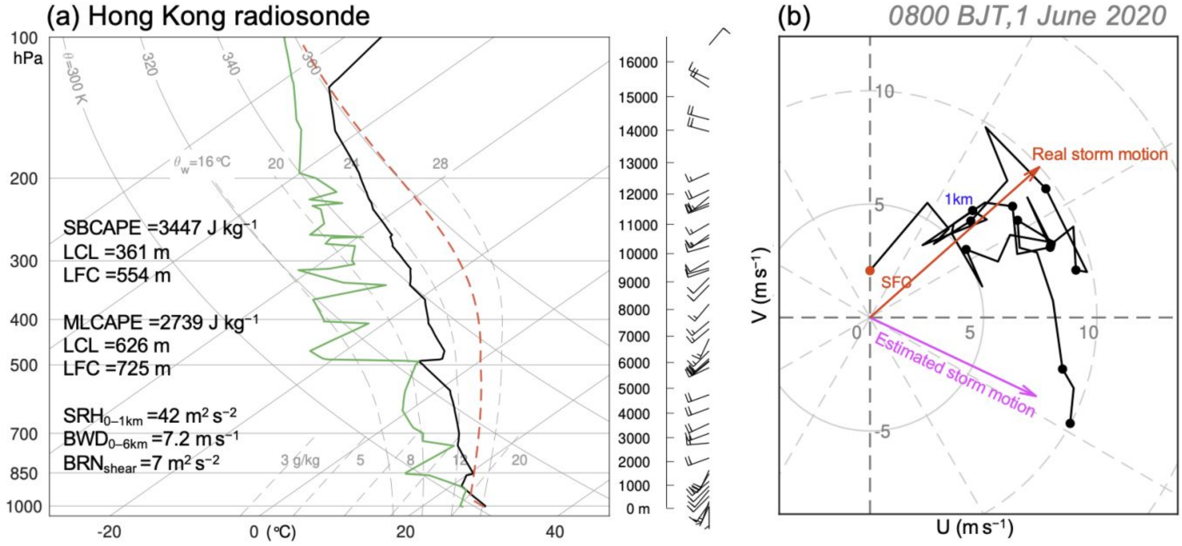


**Fig. 5.** (a) Skew *T*–log *p* diagram showing the Hong Kong sounding launched at 0800 BJT on 1 June 2020. The ambient temperature and dewpoint are represented by the solid black and green lines, respectively. The parcel that ascends undiluted from the surface is indicated by the dashed red curve (without virtual temperature correction). The half barb and full barb represent 2 and 4 m $s^{-1}$, respectively. (b) Hodograph diagram plotted by the horizontal winds in (a). The red and magenta arrows represent the observed storm motion and the computed storm motion by the method proposed by Bunkers (2000). The surface level is denoted by red dot.

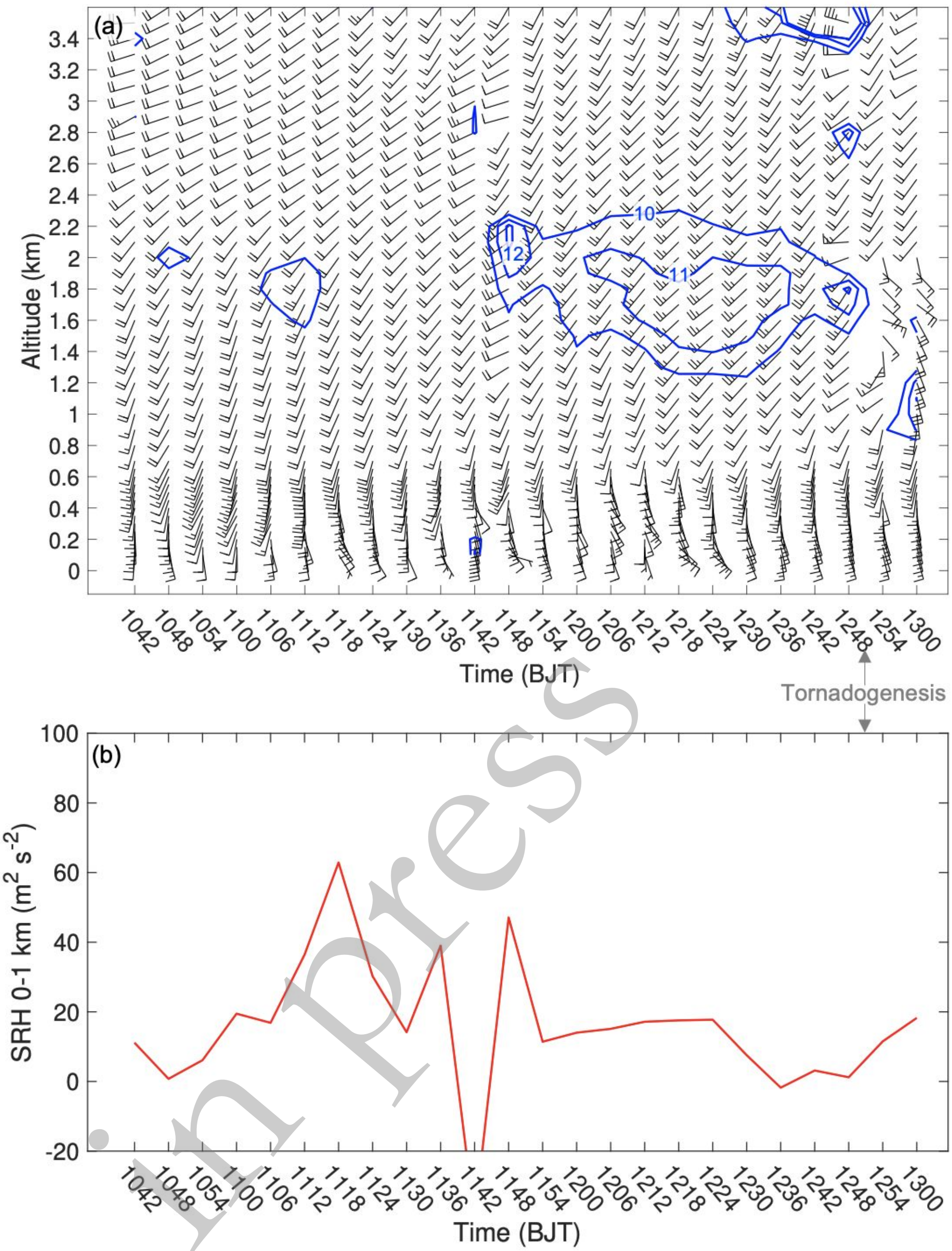




**Fig. 6.** (a) Horizontal winds (barbs) observed by the wind-profiling radar as described in Fig. 1c. The wind speeds are contoured in blue from 10 m s$^{-1}$. (b) The 0–1 km SRH calculated using the wind profiles in (a) from 1042 to 1300 BJT on 1 June 2020. The observed storm motion is used to calculate the SRH value.

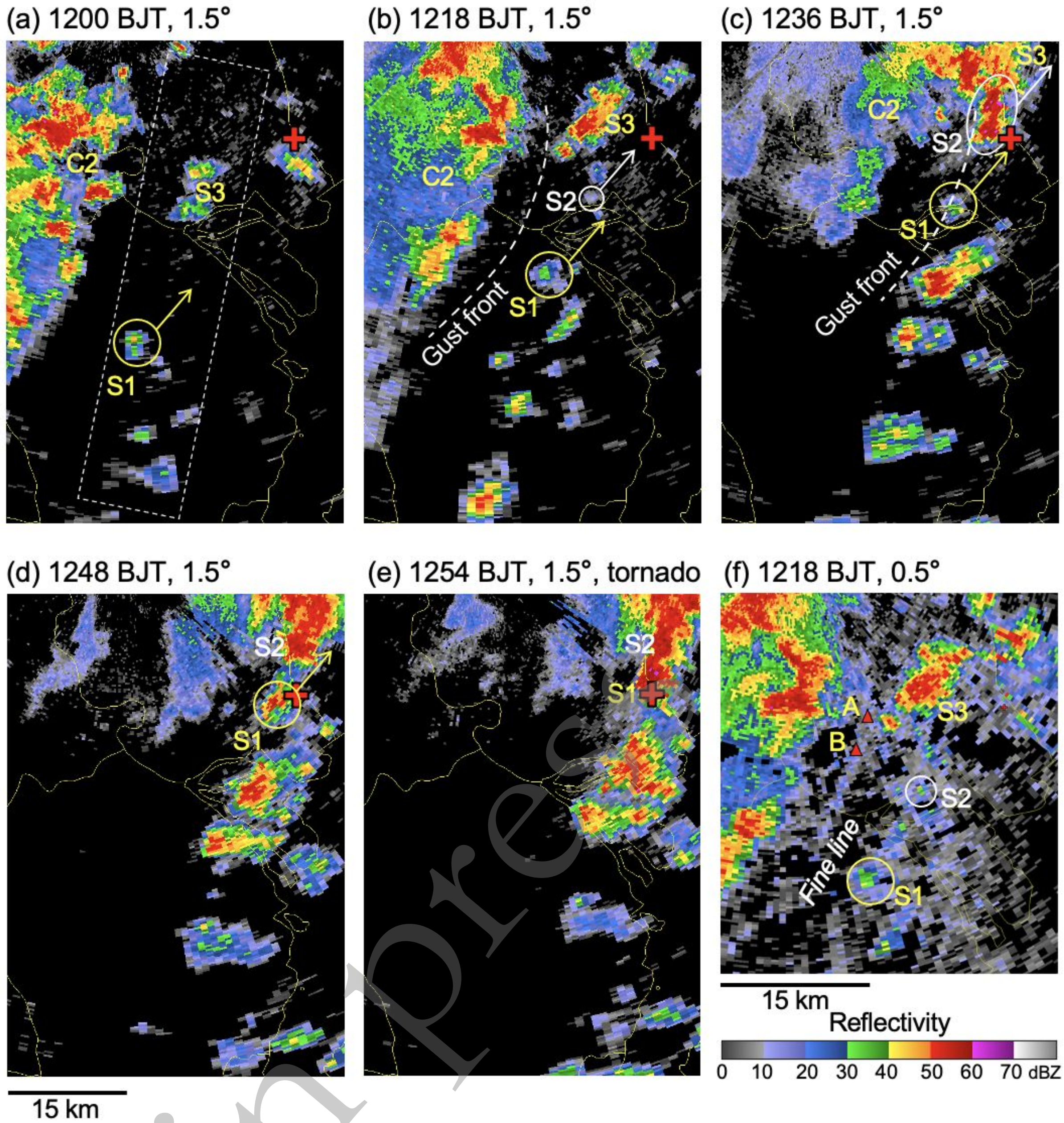


**Fig. 7.** Radar reflectivity at different elevation angles from the S-band operational radar as described in Fig. 1c. The red cross marks the approximate location of the tornado. The arrows represent the moving directions of the circled storms. The dashed curve in (b) marks the location of the gust front identified based on the fine line at the lowest radar level, as shown in (f). The hook echo region at the 0.5° elevation angle at 1254 BJT is enlarged in (g). Triangles A and B shown in (f) represent the locations of the surface weather stations used in Fig. 8.

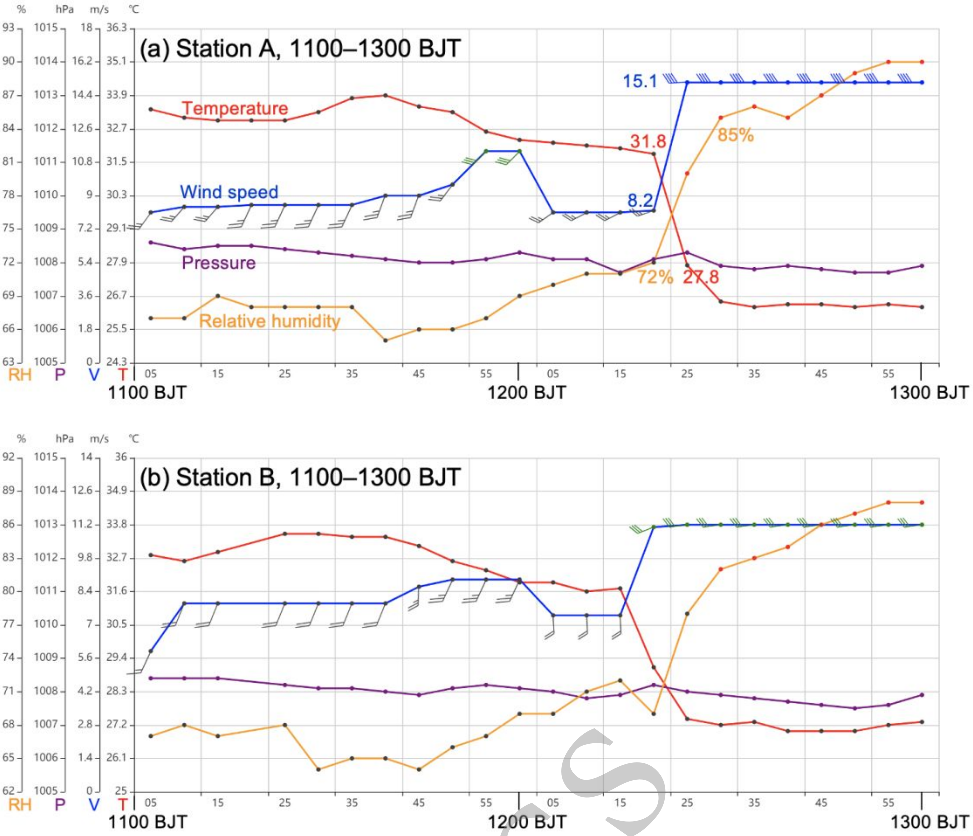


**Fig. 8.** Time series of surface temperature (red), wind speed (blue), pressure (purple) and relative humidity (orange) on 1 June 2020 obtained from surface weather Stations A and B, as shown in Fig. 7f. The half barb and full barb represent 2 and 4 m $s^{-1}$, respectively.

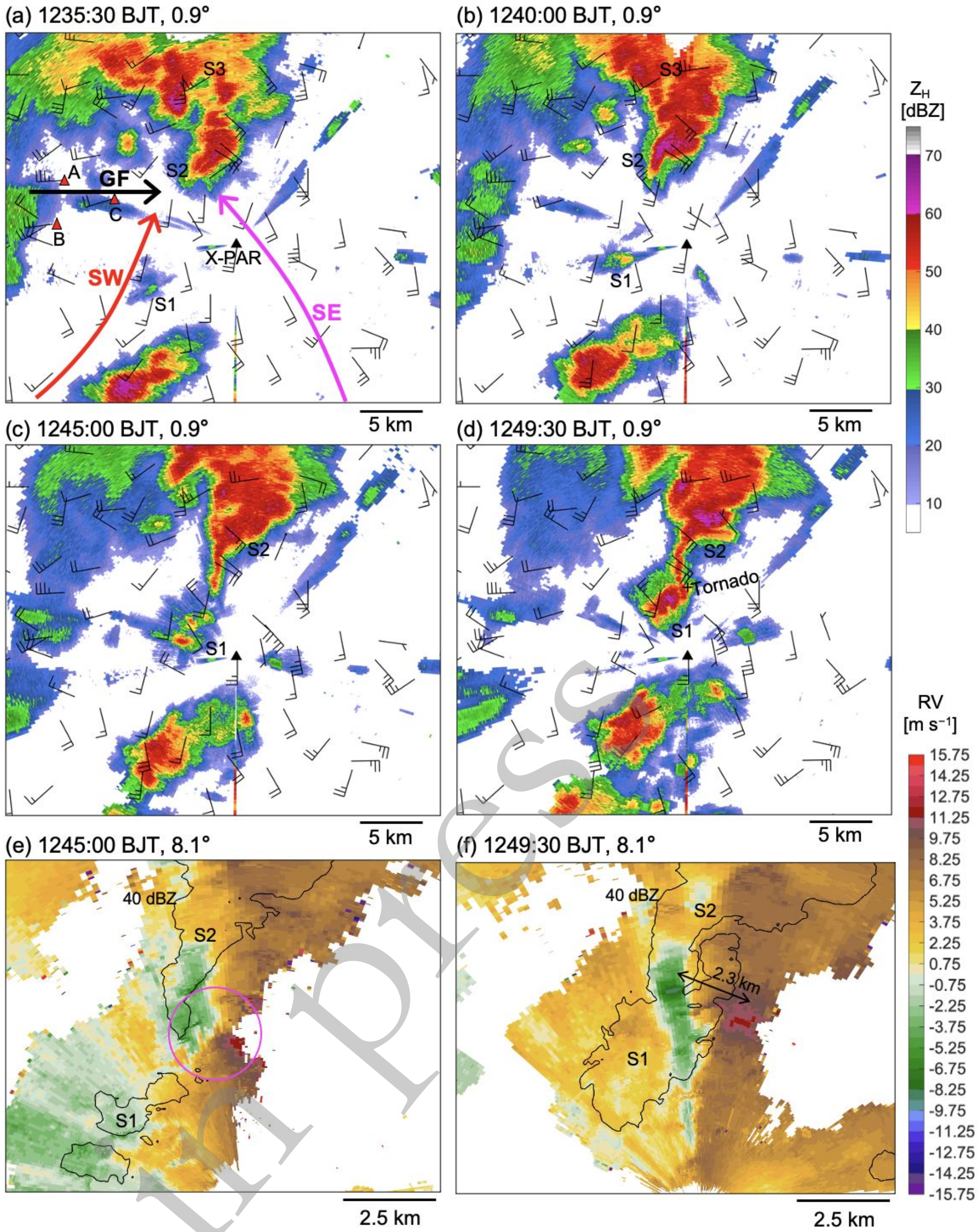




**Fig. 9.** (a)–(d) Reflectivity at the 0.9° elevation angle from X-PAR (black triangle) as described in Fig. 1b. The overlaid surface winds (barbs) are valid at (a) 1235, (b) 1240, (c) 1245 and 1250 BJT on 1 June 2020. The half barb and full barb represent 2 and 4 m s$^{-1}$, respectively. The black cross in (d) denotes the tornado location. (e),(f) Radial velocity at the 8.1° elevation angle from the X-PAR, showing the mesocyclone signature (refer to the magenta circle) near the hook echo. The black, red and magenta arrows in (a) represent the direction of cold outflows

(GF), southwesterly monsoonal flows (SW) and southeasterly monsoonal flows (SE), respectively, as described in the text. Surface weather stations marked by red triangles are labeled by A, B and C.

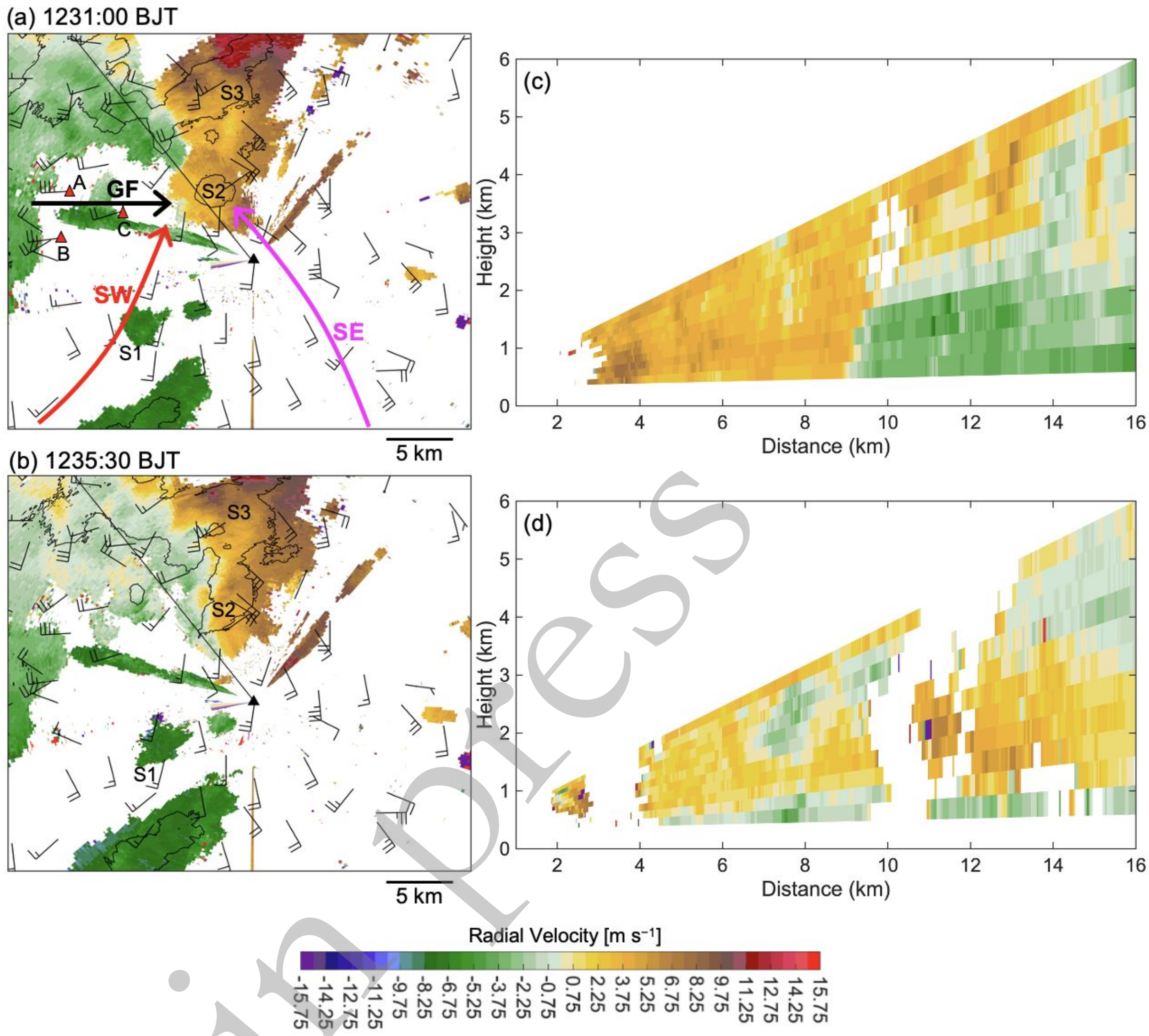




**Fig. 10.** (a),(b) Radial velocity at the 0.9° elevation angle from the X-PAR (black triangle) as described in Fig. 1b. The overlaid surface winds (barbs) are valid at (a) 1230 and (b) 1235 BJT on 1 June 2020. The half barb and full barb represent 2 and 4 m $s^{-1}$, respectively. The reflectivity is contoured as 40 dBZ in black. The arrows and red triangles are the same as those in Fig. 9a. (c),(d) Vertical cross-sections of radial velocity along the black lines in (a) and (d), respectively.

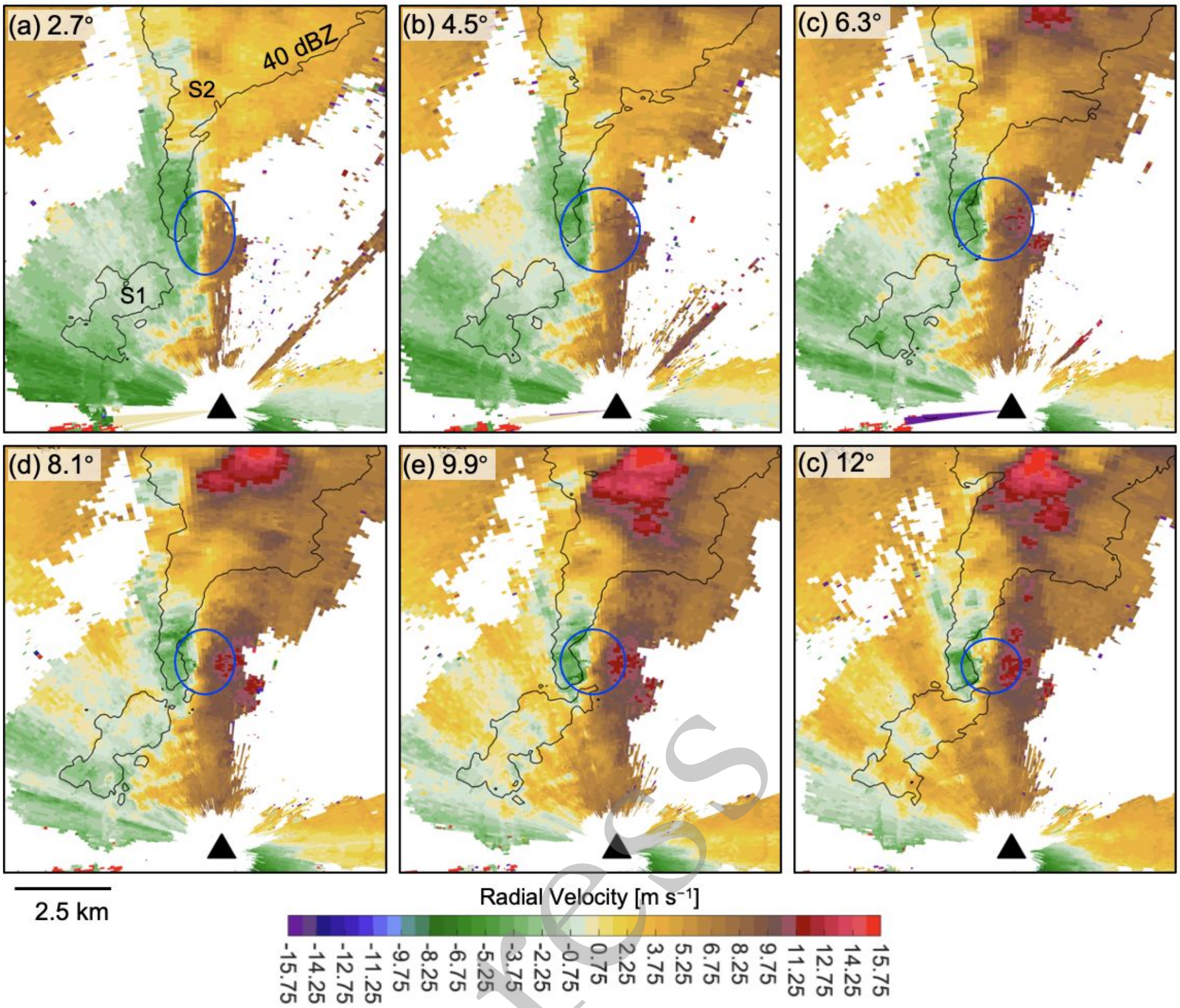


**Fig. 11.** Radial velocity at different elevation angles from the X-PAR (black triangle) at 1246:30 BJT on 1 June 2020. The 40-dBZ reflectivity is contoured in black. The mesovortex signatures are manually marked by blue ellipses.

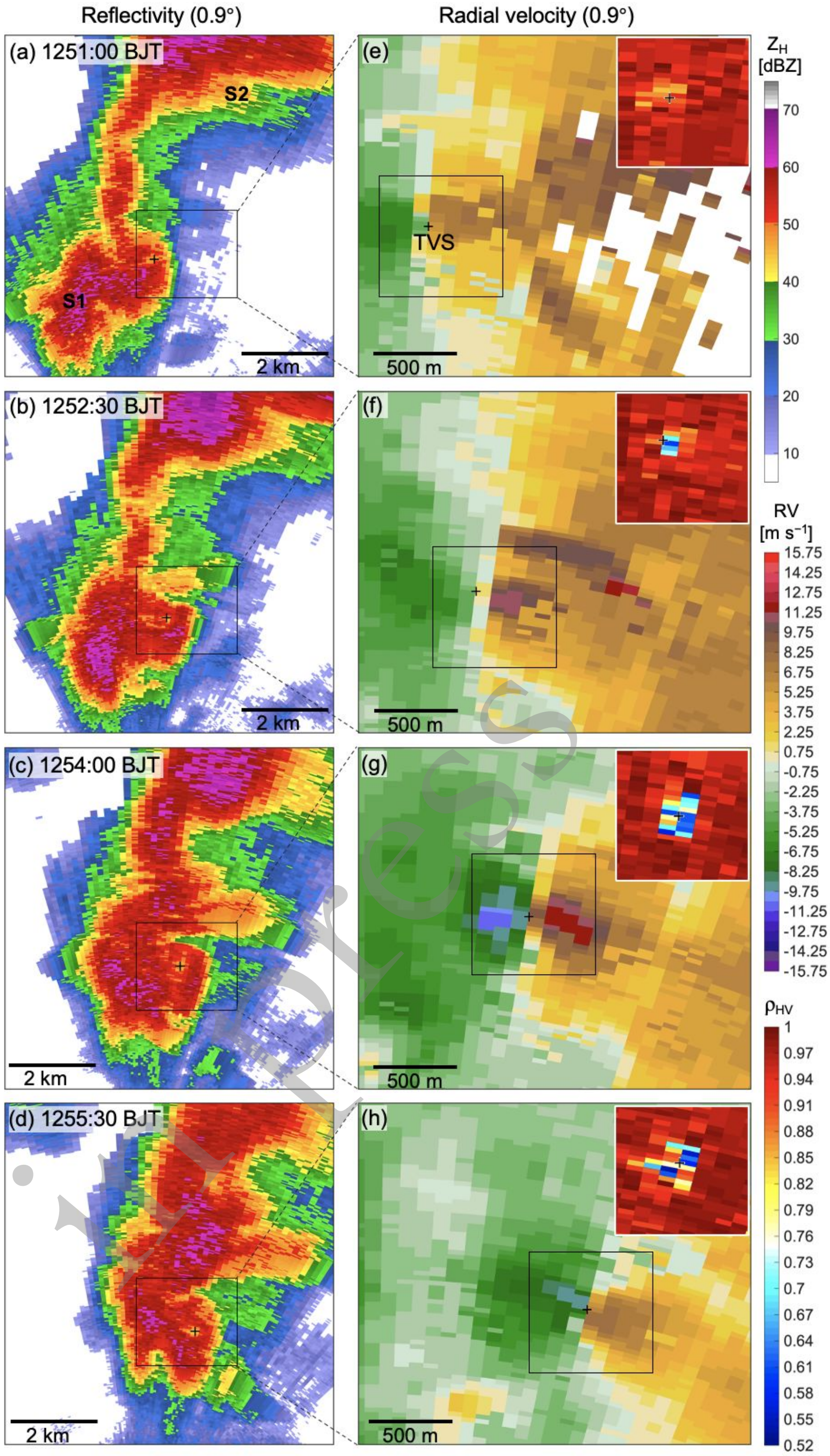


**Fig. 12.** (a)–(d) Reflectivity at the 0.9° elevation angle from X-PAR at different times on 1 June 2020. (e)–(h) The 0.9° radial velocity enlarged in the rectangle area around the hook echo.

The centroid of TVS is marked by a cross. The copolar cross-correlation coefficient ($\rho_{HV}$) around TVS (within the rectangle) is also shown in the upper-right corner.

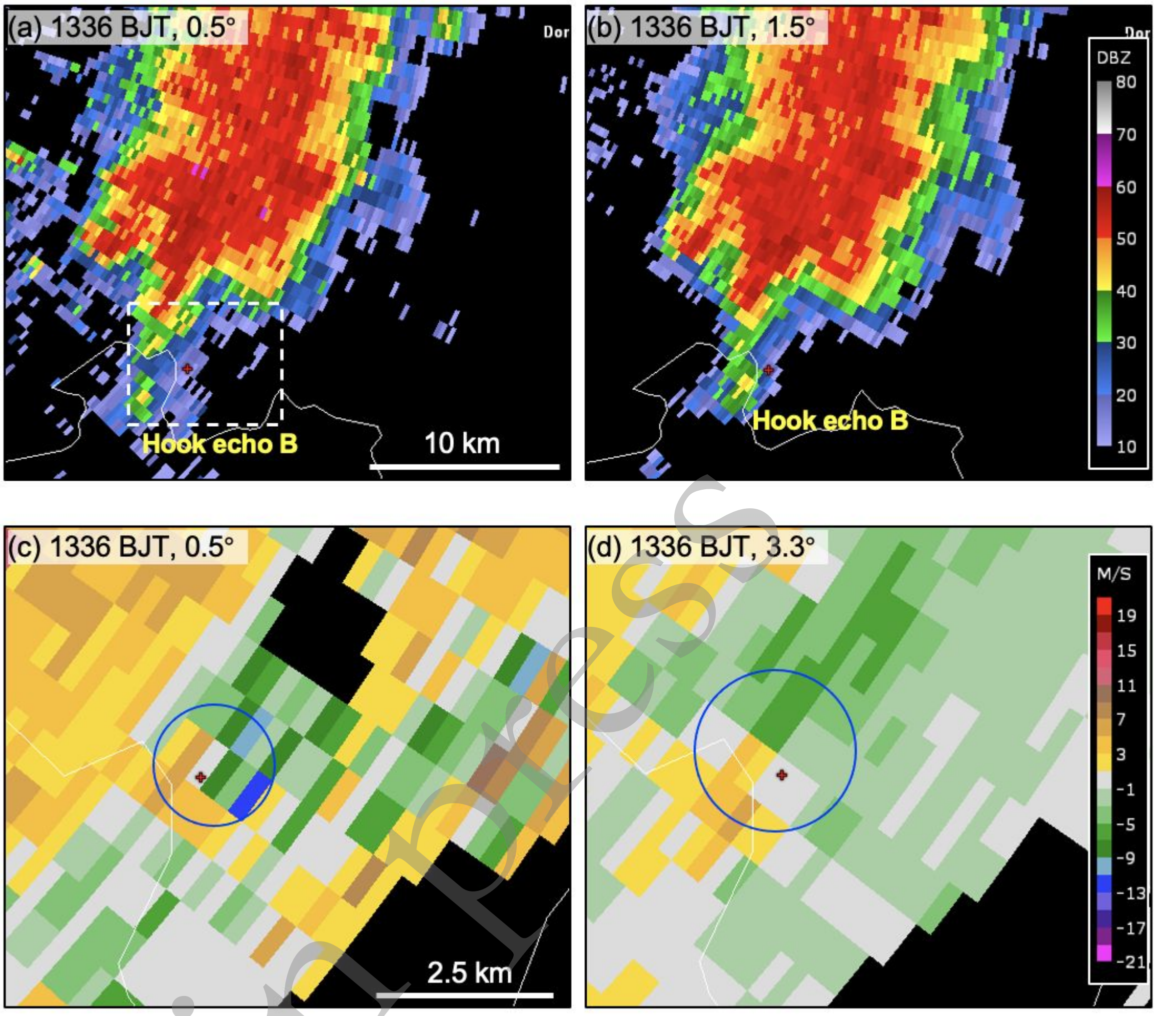


**Fig. 13.** (a),(b) Radar reflectivity from the S-band operational radar valid at 1336 BJT on 1 June 2020. (c),(d) Radial velocity around the hook echoes and the low-level mesovortex (blue circle) within the dashed box in (a). The red crosses are plotted for location reference.

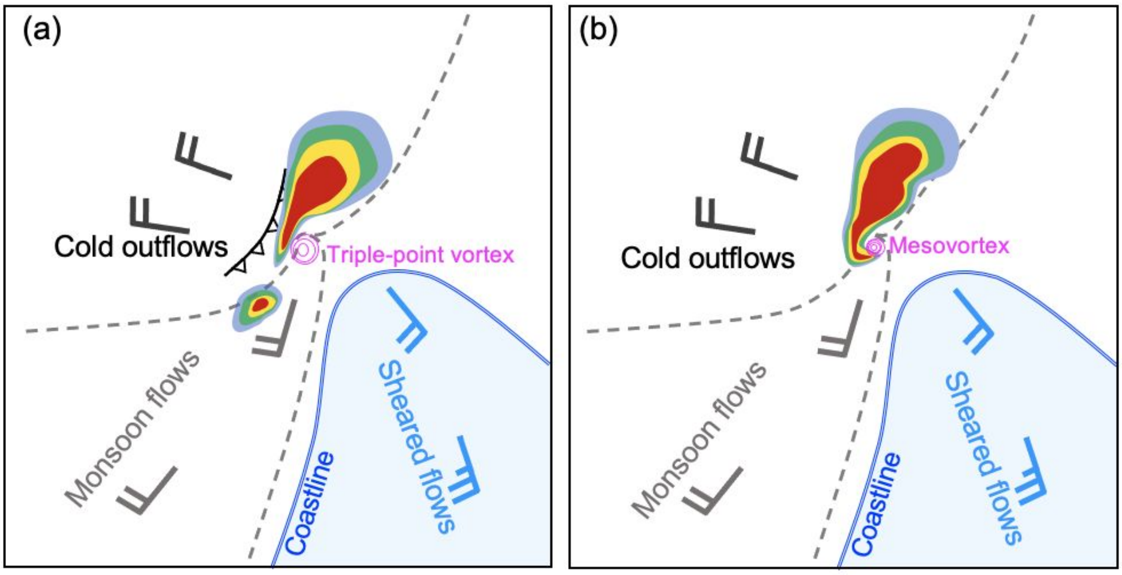


**Fig. 14.** Schematic of the mesovortex formation within a storm (shaded in multiple colors) occurring over the estuary of PRD. Dashed curves represent the surface boundaries associated with the storm-generated outflows (black barbs) and southwesterly (gray barbs) and sheared (blue barbs) monsoonal onshore flows. The enhanced vertical vorticity near the triple point is marked in magenta. The outflow boundary appears as a curve with triangles. The blue shading represents the PRD water surface.